Stanford Exploration Project, Report 79, November 16, 1997, pages 1–216

Time-lapse seismic reservoir monitoring: The petrophysical basis

David Lumley, Jack Dvorkin[1] *and Amos Nur*[1] [1]

keywords: *impedance, production, modeling, prestack, rock physics, noise, elastic, amplitudes*

ABSTRACT

Time-lapse seismic monitoring of subsurface rock property changes incurred by reservoir production processes is increasingly being proposed as a new diagnostic tool in efficient reservoir characterization and management. We perform a model study to simulate waterflood production in a light oil reservoir of Ottawa sand, and generate synthetic time-lapse monitor seismic data both pre-flood, and at two subsequent waterflood phases. Pore pressure and oil/water pore saturation levels are simulated in the reservoir due to two water injection well galleries by diffusive fluid-flow modeling. The pressure and saturation data are converted to rock density and both bulk and shear moduli, using rock physics calibration curves derived from laboratory data. Synthetic seismic reflection data are generated from the resulting spatially variable rock physics properties at three separate waterflood stages. In the presence of realistic noise levels, stacked and prestack migrated reflection images clearly show the extent of the water-invaded zone after production. Furthermore, we apply a prestack seismic impedance inversion method and accurately track the relative P and S elastic impedance changes in the reservoir rock caused by the varying petrophysical conditions associated with the waterflood production process.

INTRODUCTION

Hydrocarbon reservoirs are increasingly recognized as spatially heterogeneous entities in terms of pore-fluid content, pore-fluid saturation, porosity, permeability, lithology, and structural control. Knowledge of these reservoir parameters and their spatial variation is critical in the evaluation of the total volume of hydrocarbon reserves in place, in understanding and predicting physical processes in the reservoir such as fluid

[1]**email:** not available
[1]Stanford Rock Physics and Borehole Geophysics Project, Stanford University.

flow and heat transfer, and in projecting and monitoring reservoir fluid production and recovery as a function of time.

Conventional approaches to estimating reservoir properties are mainly obtained through borehole measurements such as: rock cores, rock cuttings, geophysical well logs, and reservoir engineering pressure tests. These data are valuable in that they represent *in situ* measurements, but unfortunately only sample a very small fraction of the total reservoir volume [e.g., Nur, (1989)].

Surface seismic data, on the other hand, potentially sample the entire reservoir volume, although at a lower resolution and in a *remote*, as opposed to in situ, manner. Traditionally, surface seismic data are used as an imaging tool to make seismic-derived geologic maps of the reservoir target zone. These images are subsequently interpreted by reservoir geologists in terms of structure, stratigraphy, and major fault patterns, in order to provide some structural control to the reservoir model. However, relatively little work has been done to relate seismic reflection data directly to the reservoir mechanical property contrasts that develop due to hydrocarbon recovery.

Furthermore, a new diagnostic role for seismic has been proposed recently, in which several repeat seismic surveys are acquired in time-lapse mode to monitor reservoir production processes. This concept offers a method for better characterization of reservoir complexity by monitoring the flow of fluids with time in a producing reservoir. Additionally, monitoring provides a full reservoir volume analysis of production sweep efficiency, early prediction of injectant breakthrough, and location of bypassed (unproduced) hydrocarbons. Seismic monitoring of reservoir processes potentially offers a new dimension to the manner in which hydrocarbon reservoirs are currently developed and produced.

Previous work

Although the concept of time-lapse reservoir monitoring is relatively recent, a few notable pilot projects have been attempted. Pullin et al. (1987) collected two 3-D seismic surveys before and after a steam pilot at an Athabasca tar sands reservoir site. By comparing time delay and amplitude attenuation difference maps between the two surveys, Pullin et al. seemed to be able to map the presence of steamed versus unsteamed zones. The time delays and amplitude attenuation through steamed sections of reservoir compared reasonably well with prior rock physics laboratory studies of the predicted thermal effects on seismic data.

Greaves and Fulp (1987) designed and analyzed a 3-D seismic monitoring experiment of an in situ combustion (fireflood) EOR process. They collected three 3-D surface seismic data sets: one pre-combustion and two during combustion. They made stacked sections from each survey and computed traveltime and amplitude difference maps comparing each fireflood data set to the pre-fire base survey. They were able to monitor the volume of combustion burn accurately, as well as its sweep efficiency using these maps, as confirmed by subsequent borehole measurements.

More recently, Graebner (1993) presented results of a 3-D marine seismic monitoring survey in the Oseberg field offshore Norway. The objective was to monitor the movement of the gascap during production over time. They compared reservoir fluid flow simulation predictions of the gas-oil contact to the actual seismic observations, and found a seismic amplitude anomaly in the difference section which corresponded to the zone of change predicted by the fluid-flow simulator. Unfortunately, their results may not be conclusive due to significant noise in the final seismic difference sections, and concerns about relative and absolute survey positioning errors from one survey to the next.

Outline

In this paper, we present what we believe to be a major step forward in establishing the petrophysical basis for reservoir monitoring by conducting a comprehensive physical modeling study combining fluid flow simulation and rock physics with seismic imaging and impedance estimation. The paper proceeds as follows. For a simple but realistic reservoir model, we compute the pore pressure and oil/water saturation spatial distributions for two water injection well galleries in a light-oil bearing Ottawa sand reservoir, based on simple fluid-flow theory. These fluid-flow parameters are then mapped through laboratory-measured rock physics relationships to predict the resulting spatial distributions of rock bulk and shear moduli, and density. This process is repeated at three distinct phases of waterflood. We then input the rock physics seismic parameters to a Kirchhoff synthetic seismogram modeling code to simulate both a pre-flood seismic base survey, and two subsequent waterflood surveys. In the final analysis section, we make stacked and prestack migrated difference sections which clearly show the extent of each phase of the waterflood, and make elastic impedance estimates which accurately assess the change in petrophysical properties in the reservoir due to the waterflood process.

FLUID-FLOW SIMULATION

We assume a simple model of diffusive fluid-flow in this study. We simulate the fluid flow response of two water injection well galleries in a thin (50 m thick) horizontal reservoir at 2 km depth. Please refer to Figure **??** for the well gallery production geometry.

Initially, the reservoir is assumed to be 100% saturated with light oil in a consolidated Ottawa sand of 33% porosity. Clearly this is an idealized case in which the connate water saturation S_{wc} is zero. After some characteristic time period of water injection, we calculate the pore pressure and water saturation as a function of distance from the injection wells. Assuming isothermal diffusive flow in a thin homogeneous reservoir of constant permeability k, and water and oil of homogeneous (but different) viscosity, both the pore pressure P_p and water saturation S_w can be

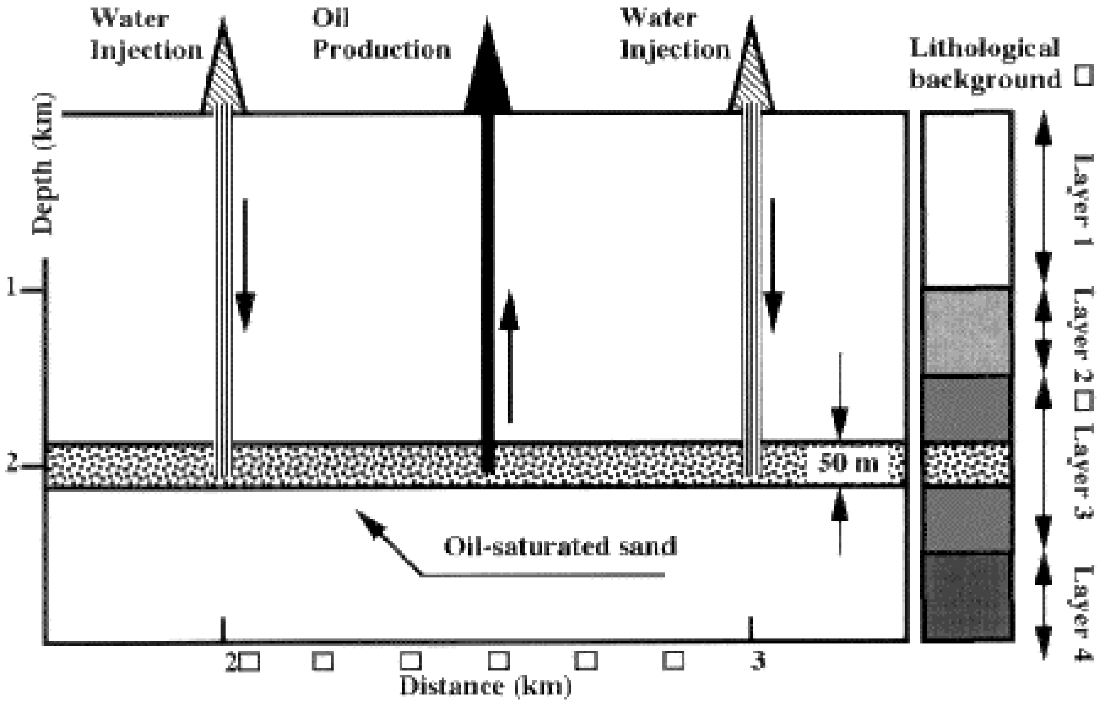

Figure 1: Reservoir production geometry. Two well galleries (lines of injecting wells in the direction perpendicular to the plane of the page) inject the waterflood, and a central line of wells produces the oil. The Ottawa sand reservoir is at a depth of 2 km and is 50 m thick. david2-waterflood [NR]

modeled as simple diffusion:

$$P_p(r,t) = \frac{P_w}{2\sqrt{\pi\kappa_p t}} e^{-x^2/4\kappa_p t} \; , \tag{1}$$

$$S_w(r,t) = \frac{1}{2\sqrt{\pi\kappa_s t}} e^{-x^2/4\kappa_s t} \; , \tag{2}$$

where P_w is the pressure with which the water is being injected, and κ_p, κ_s are the effective diffusivities for the pressure and water saturation fronts, which are related to each other and depend on reservoir permeability k and fluid viscosity η. The horizontal distance from the injection well is denoted as x. We consider the fluid flow to be scale invariant in that the fluid will diffuse a characteristic distance x' away from the injector in a characteristic time t' given by the skin depth diffusion relation:

$$x' \approx \sqrt{\kappa t'} \; . \tag{3}$$

Dake (1978, p. 352) gives the physical conditions for which diffusive fluid flow is a valid approximation:

- When displacement occurs at very high injection rates so that the condition of vertical equilibrium is not satisfied and the effects of the capillary and gravity forces are negligible.
- For displacement at low injection rates in reservoirs for which the measured capillary transition zone greatly exceeds the reservoir thickness, and the vertical equilibrium condition applies.

Under either of these conditions, we can simulate Gaussian distributions of pore pressure and water saturation. Additionally, since pressure and water saturation change much more quickly than reservoir temperature, we assume that the waterflood is an isothermal process. These approximations are justified because in this study we concentrate on the principal possibility of the seismic detection of production-associated changes in the reservoir, rather than on the detailed nature of reservoir fluid flow simulation.

PETROPHYSICAL PROPERTIES

Given the distribution of pore pressure and water saturation as functions of time and distance from the water injectors, we predict the associated compressional (P) and shear (S) seismic velocities V_p, V_s and density ρ throughout the reservoir at two stages of waterflood.

The Stanford Rock Physics and Borehole Geophysics Project (SRB) has conducted several lab measurements of dry and saturated rocks at various pressures, temperatures, and for variable pore-fluid saturants. Figure **??** shows some of the SRB lab results for the Ottawa sand on which our reservoir study is based. The curve labeled "GAS" was obtained by measuring the bulk and shear moduli K and μ on an oven-dry sample of Ottawa sand, at a confining pressure P_c of 51 MPa, at a reasonable reservoir temperature of about 50 $^\circ$C. The fluid curves (water and oil) are calculated from the dry data by means of the Gassmann fluid substitution equation in order to predict the 100% fluid-saturated bulk and shear moduli for the Ottawa sand for both hot oil and hot water as injectants. This procedure is valid for predicting low frequency velocities such as those encountered by surface seismic reflection data.

Gassmann's Equation relates dry elastic moduli to fluid-saturated elastic moduli. For bulk moduli, Gassmann (1951) found that

$$K_s = \frac{K_m \cdot M}{1 + M} \ , \tag{4}$$

where M is a normalized ratio of mineral, fluid and dry bulk moduli such that

$$M = \left(\frac{K_d}{K_m - K_d} + \frac{K_f}{\phi(K_m - K_f)} \right) \ . \tag{5}$$

Equation (4) is a rearrangement of Equation 2.77 from Bourbié et al. (1987). Concerning shear moduli, Gassmann found no distinction between dry and saturated properties:

$$\mu_s = \mu_d \ . \tag{6}$$

In the above expressions, K_m is the bulk modulus of the pure mineral skeleton, K_f is the bulk modulus of the saturating fluid, and K_d is the bulk modulus of the dry rock under study. K_s is the Gassmann theoretical bulk modulus of the dry rock after complete saturation with wetting fluid. Similarly, μ_s is the Gassmann theoretical shear modulus predicted to be the same as the dry bulk shear modulus μ_d. The underlying assumptions in Gassmann's Equation are:

- the rock satisfies linear isotropic elasticity,
- the rock skeleton is comprised of one single homogeneous mineral phase,
- the wetting fluid is homogeneous and completely saturates the porosity,
- the porosity ϕ is uniform throughout the sample, and
- the measurements are made at low frequency (quasistatic).

Figure **??** shows the resulting P-wave velocity versus pore pressure paths for Ottawa sand under various types of reservoir production processes. For our study, we consider the "waterflood" process, labeled A, A'. Figure **??** shows that there is a net increase in V_p of about 10% as water is injected to increase effective reservoir pore pressure, and hot oil is replaced with hot water. Given the pore pressure and water saturation data from the fluid flow simulation, we use the dry data in Figure **??** and the Gassmann relation (4) to predict the partially saturated shear and bulk moduli as a function of distance from the water injection well. Given the predicted $K_s(r,t)$ and $\mu_s(r,t)$, we calculate the P and S low frequency seismic velocities as:

$$V_p^{sat} = \sqrt{\frac{K_s + 4\mu_s/3}{\rho_s}} \, , \tag{7}$$

and

$$V_s^{sat} = \sqrt{\frac{\mu_s}{\rho_s}} \, , \tag{8}$$

where the subscript "s" refers to a saturated quantity.

Using this technique, we calculate pore pressure, water saturation, P-wave velocity, S-wave velocity and density, as a function of distance from the well and injection duration time, in an Ottawa sand reservoir at 50 $^{\circ}$C under two phases of waterflood injection.

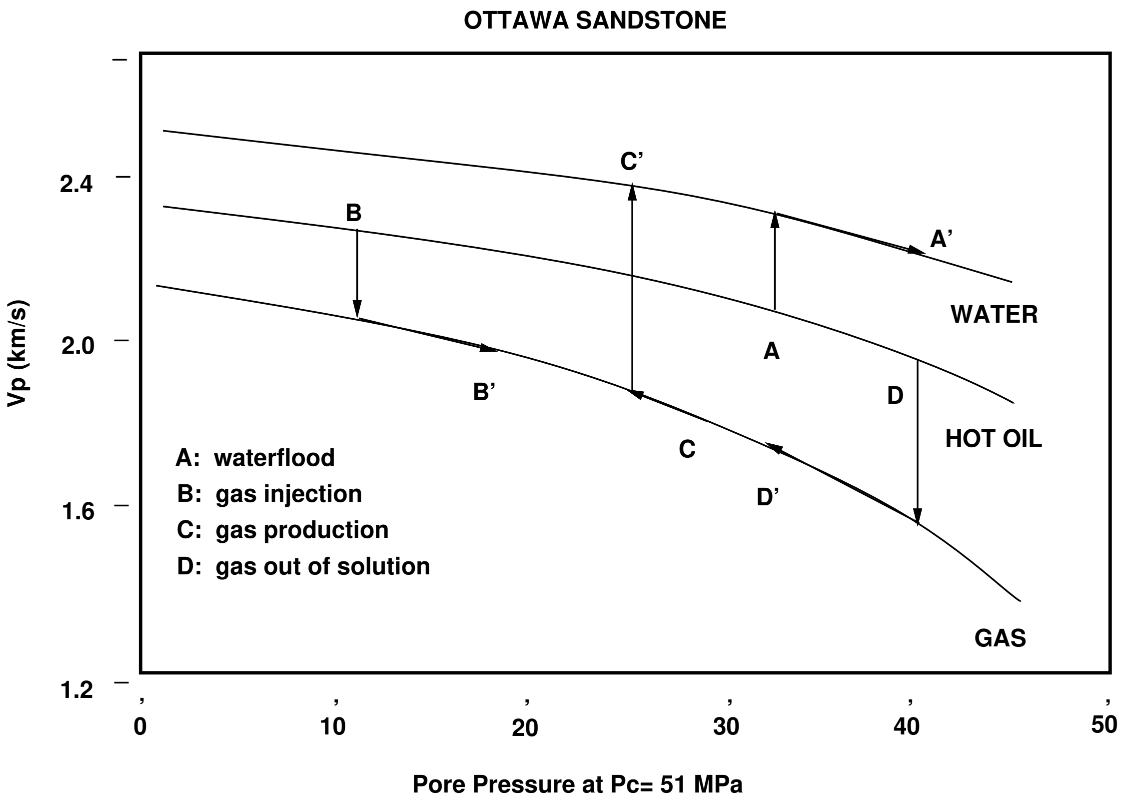

Figure 2: Petrophysical laboratory data, and saturated rock predictions for various reservoir production processes, in Ottawa sand. The dry rock data (lower curve) are taken from Han (1986). david2-labdata [NR]

RESERVOIR MODELS

Using the techniques described in the sections on fluid-flow simulation and petrophysical property prediction, we calculate three elastic models at three phases of waterflood production: pre-flood, at one characteristic time step of waterflood, and after two characteristic time steps of waterflood.

Petrophysical properties

The background values and the geometry of the reservoir model are plotted in Figure **??**. The reservoir is 50 m thick and the top of the reservoir is at 2 km depth. We simulate water injection wells located at 2 km and 3 km respectively. Table 0.1 lists the pre-flood and post-flood petrophysical properties at an injection well. The background properties both above and below the reservoir are: V_p = 2.38 km/s, V_s = 1.13 km/s, and ρ = 2.1 g/cc. The relative P impedance contrast is calculated as:

$$\zeta_p = \frac{2(\rho^+ V_p^+ - \rho^- V_p^-)}{(\rho^+ V_p^+ + \rho^- V_p^-)} \,, \tag{9}$$

and similarly for the relative S impedance contrast:

$$\zeta_s = \frac{2(\rho^+ V_s^+ - \rho^- V_s^-)}{(\rho^+ V_s^+ + \rho^- V_s^-)} \,, \tag{10}$$

where "+" superscripted properties refer to the layer below the interface, and "-" superscripted properties refer to the layer above the interface. We note that ζ_p and ζ_s are exactly twice the normal incidence P and S plane-wave reflection coefficients R_p and R_s:

$$R_p = \frac{1}{2}\zeta_p \,, \tag{11}$$

$$R_s = \frac{1}{2}\zeta_s \,, \tag{12}$$

Figure **??** shows the depth-dependent form of the background model and the reservoir properties at an injection well, pre- and post-flood. V_s is the left-most curve, ρ in the center, and V_p to the right of each panel.

Waterflood diffusion

Figure **??** shows an enlarged version of the reservoir zone, before the onset of waterflooding. The top of the reservoir is at 2 km depth, and the reservoir is 50 m thick.

Reservoir properties		
	pre-flood	*post-flood*
V_p	2.19	2.29
V_s	1.15	1.03
ρ	2.05	2.09
R_p	-0.055	-0.020
R_s	-0.003	-0.050

Table 0.1: Reservoir petrophysical properties evaluated at the water injection well location (a) pre-flood, and (b) post-flood. V_p and V_s are P and S wave velocities (km/s), ρ is density (g/cc), R_p and R_s are the normal incidence P and S impedance plane-wave reflection coefficients at the top of the reservoir.

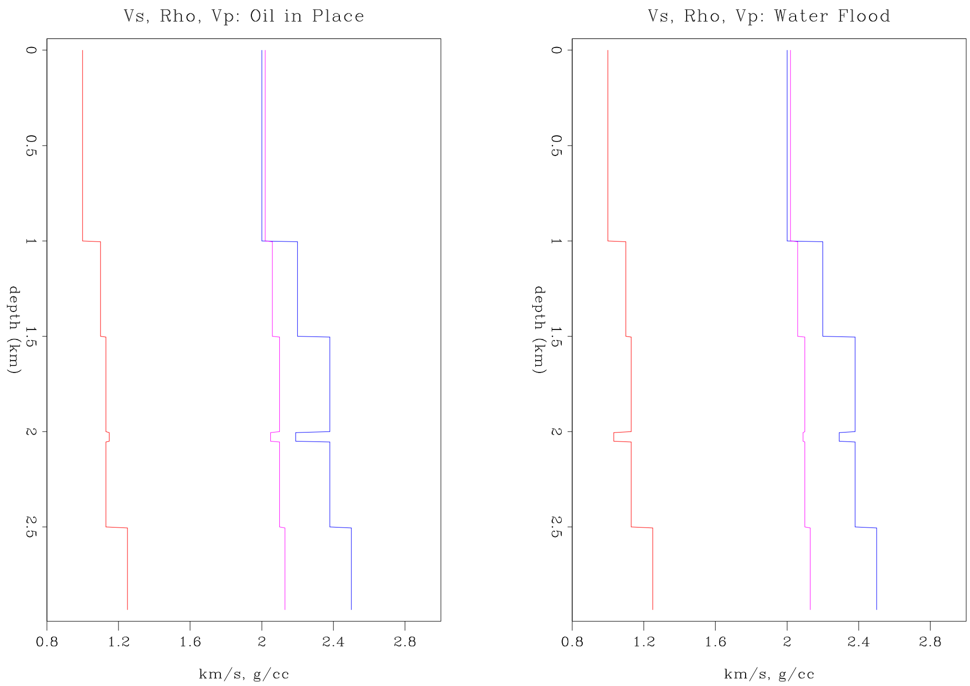

Figure 3: Depth-dependent form of the background model and the reservoir properties at an injection well, pre- (left) and post-flood (right). V_s is the left-most curve, ρ in the center, and V_p to the right within each panel. Density is nearly constant at 2.1 g/cc. $\boxed{\text{david2-curves12}}$ [CR]

Figure **??** shows the same enlargement, but after one time step of water injection. The two water injection wells are clearly located at 2 km and 3 km distance, at the centers of the water diffusion fronts. The water invaded zones (blue/grey) represent an increase in P impedance in the reservoir, with respect to the initial pre-flood reservoir conditions. Figure **??** shows the S impedance values in the reservoir after one time step of water injection. The (red/grey) water invaded zones represent a decrease in S impedance in the reservoir, with respect to the initial pre-flood conditions. Since the magnitude of shear impedance change is nearly twice as large (although opposite polarity) as the P impedance change in the water invaded zone (Table 0.1), the water injection shear impedance plume extends a larger distance away from the wells. This implies that shear waves may be more sensitive to monitoring water injection processes in light oil sand reservoirs than P waves.

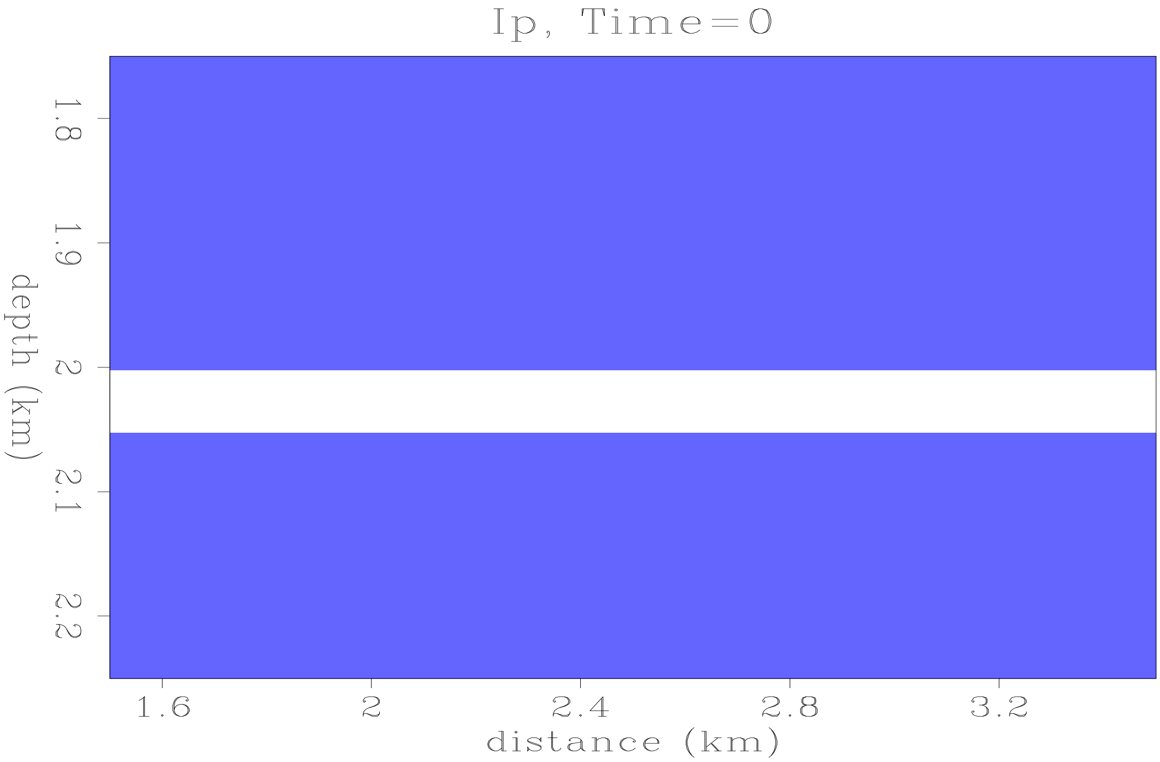

Figure 4: Pre-flood P impedance model. david2-Ip1 [CR]

Figure **??** shows the reservoir P impedance map after two time steps of waterflood. Now the P impedance diffusion front has extended about 300 m away from each injector. The (blue/grey) water invasion zone indicates a substantial increase in P impedance within the waterflood as compared to the initial reservoir conditions with 100% oil saturation in place. Figure **??** shows the S impedance map after two time steps of waterflood. Again, the S impedance front has extended about 300 m away from each injector, and its (red/grey) color indicates a decrease in shear impedance within the reservoir, at about twice the magnitude of the P impedance change, compared to the initial reservoir conditions.

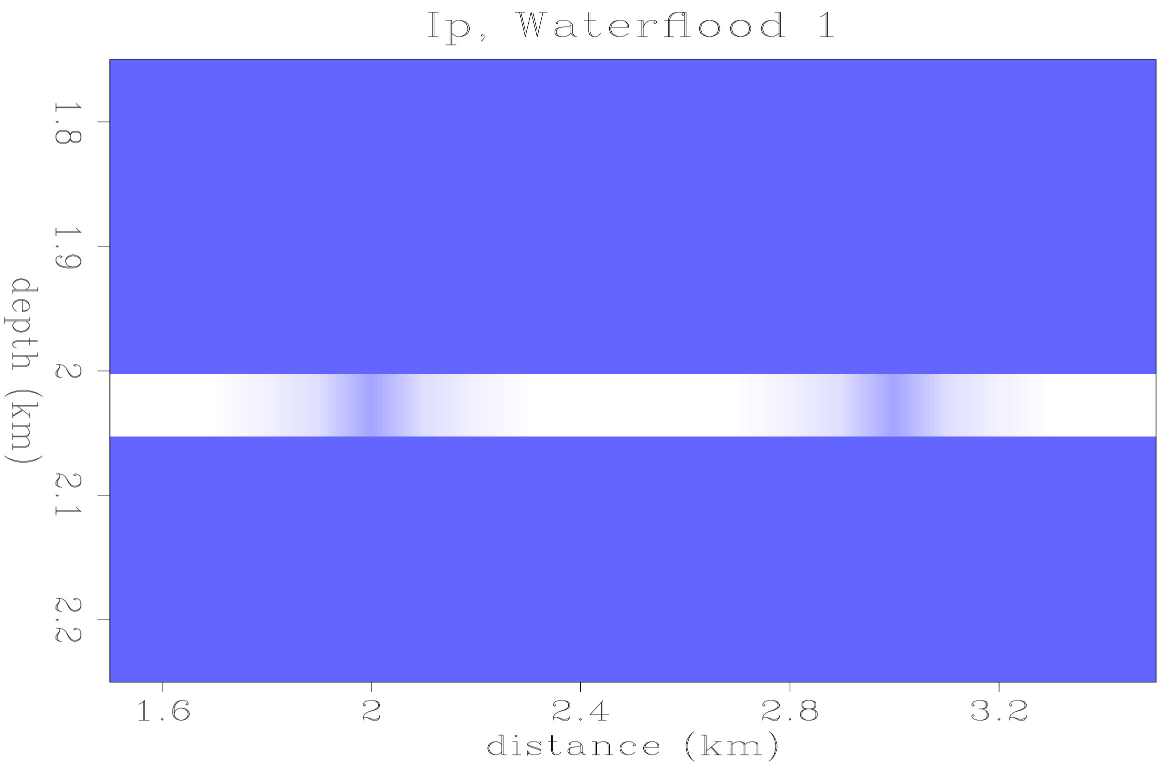

Figure 5: Waterflood 1: P impedance model. david2-Ip2 [CR]

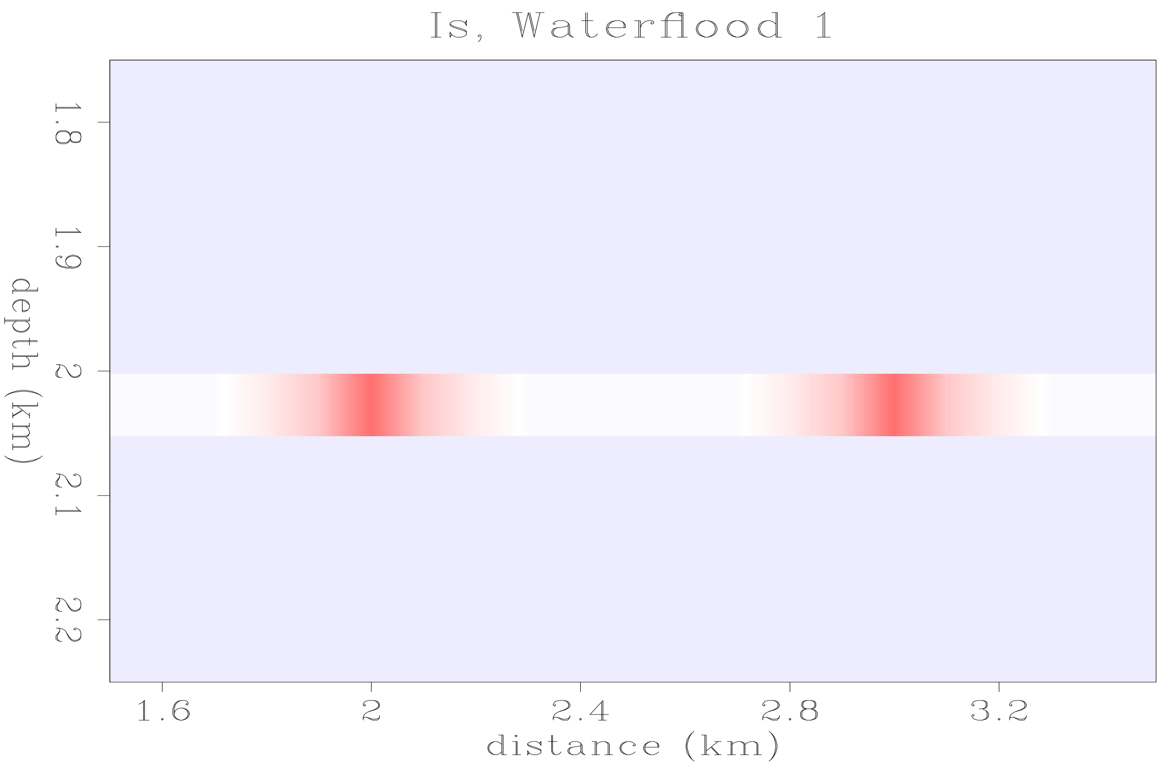

Figure 6: Waterflood 1: S impedance model. david2-Is2 [CR]

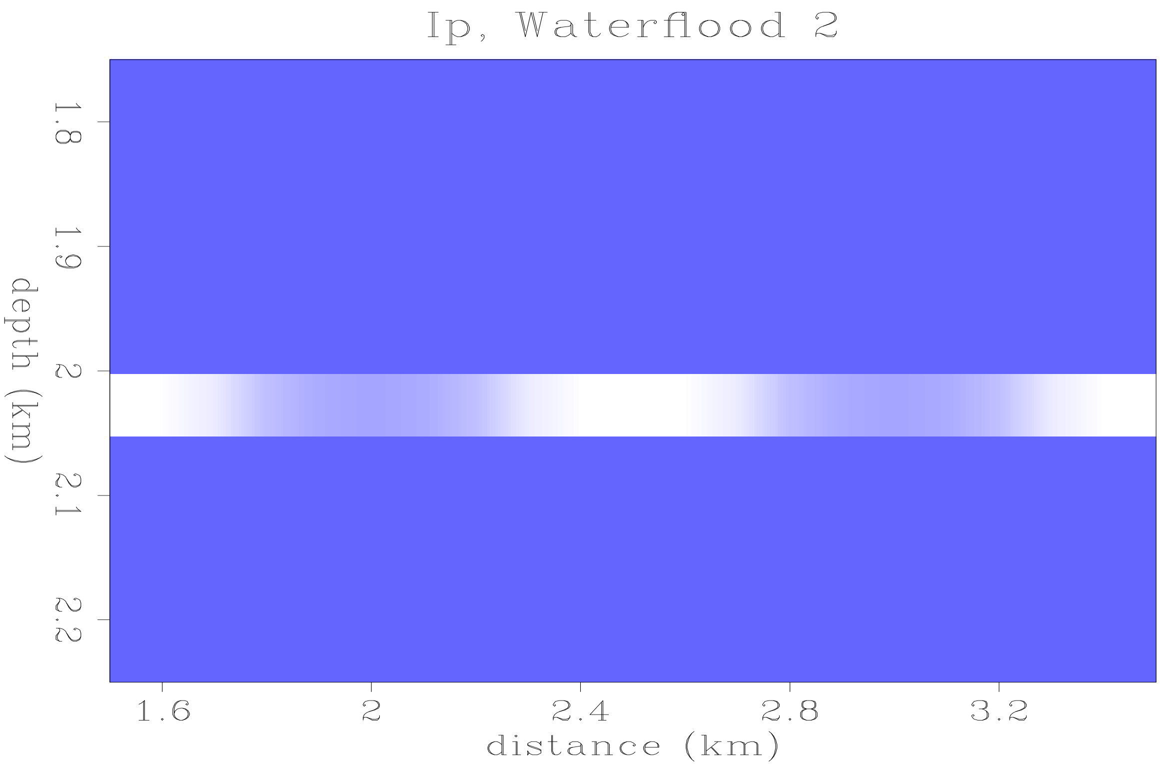

Figure 7: Waterflood 2: P impedance model. david2-Ip3 [CR]

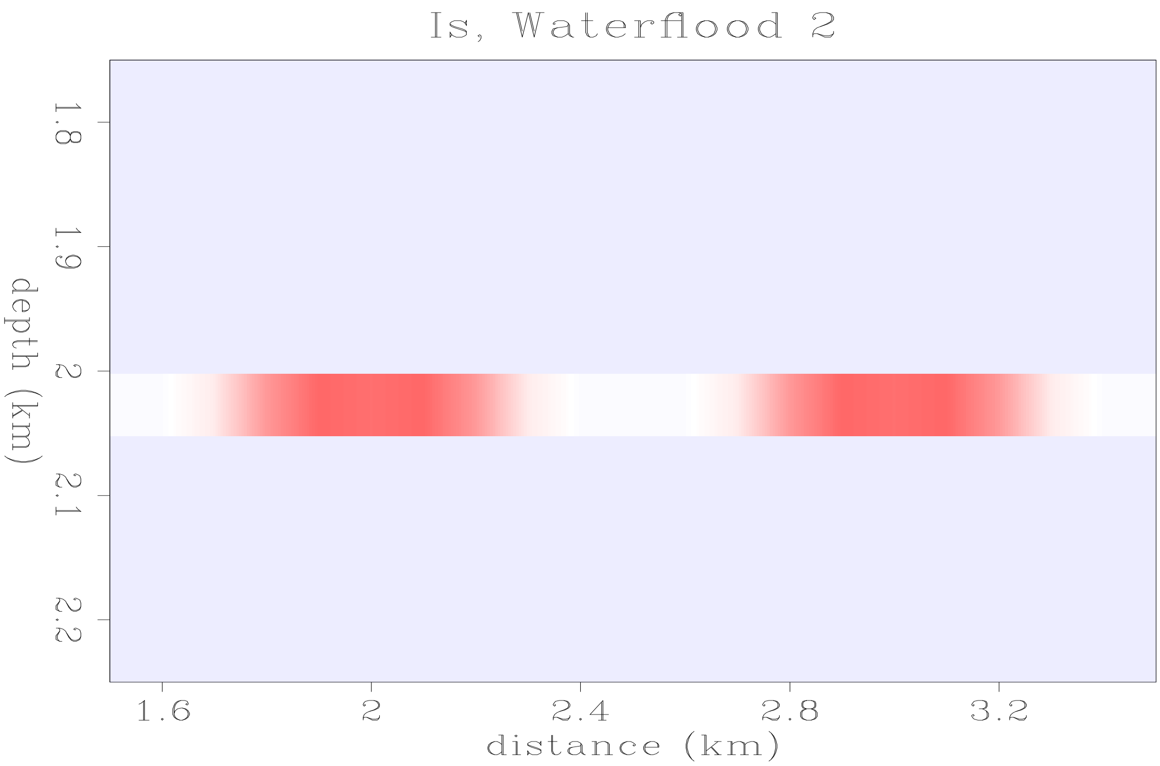

Figure 8: Waterflood 2: S impedance model. david2-Is3 [CR]

SYNTHETIC SEISMOGRAMS

Given the reservoir models both pre-flood and for each of two time steps of waterflood production, synthetic surface reflection seismic data can be generated for each time snapshot of production.

The synthetic seismograms are calculated based on the generalized Kirchhoff body force scattering theory of Lumley and Beydoun (1993). This theory combines Zoeppritz plane-wave reflection and Rayleigh-Sommerfeld elastic diffraction responses. The modeling theory can generate the correct AVO response for locally planar reflectors, and merge into diffraction where elastic properties vary spatially faster than a seismic wavelength. However, since the Green's tensors are WKBJ ray-valid, only primary reflections and diffractions are computed. Higher order multiple scattering or phenomena such as surface waves are not modeled.

The modeling theory is based on a volume integration of the body force equivalent of the $\grave{P}\acute{P}$ coefficient:

$$\hat{\mathbf{a}}_r \cdot \mathbf{u}^{P}(\mathbf{x}_r) = \int_{\mathcal{V}} ik\, A_s A_r e^{i\omega\tau_{sr}}\, \grave{P}\acute{P} \cos\phi_r \, d\mathcal{V} \ . \tag{13}$$

$\mathbf{u}^{P}$ is the P-P scattered vector wavefield measured at the receiver position $\mathbf{x}_r$, and projected onto an arbitrary receiver component direction $\hat{\mathbf{a}}_r$. A_s and A_r are the elastic WKBJ Green's function amplitudes from the source and receiver positions respectively, to each subsurface scattering point $\mathbf{x}$ in the volume $\mathcal{V}$. Similarly, $\tau_{sr} = \tau_s + \tau_r$ is the total traveltime from source to scatterer to receiver. The factor $\cos\phi_r$ is the non-geometric diffraction angle as shown in Figure **??**, and is unity along the Snell reflection path (specular), and variable otherwise. The $\grave{P}\acute{P}$ factor is the plane-wave Zoeppritz elastic P-P reflection coefficient, and k is the spatial wavenumber $k = \omega/\alpha$. The incident arrival direction vector $\hat{\mathbf{t}}^{P}$ is drawn in Figure **??**.

Figure **??** shows a noise-free synthetic CMP gather located at an injection well. The left panel is before water injection, and the right panel is after two time steps of waterflood. The reservoir reflections occur at and just below 2 seconds traveltime. In the pre-flood case, there is a strong reflection and AVO response at the reservoir. After two time steps of waterflood, the reservoir reflection is much weaker and there is almost no discernable AVO response. Figure **??** shows the same CMP gathers, but with a significant level of spatially-uncorrelated Gaussian distributed noise, filtered to the same frequency bandwidth as the signal (10–60 Hz). The S/N ratio is about 2:1 at the reservoir reflection in the pre-flood case, and about 1:1 after two time steps of waterflood. It would be very difficult to detect the reservoir reflection after waterflood alone, but the change in reflection character during time-lapse monitoring of the production process seems quite easy to detect for this geometry, petrophysical model, and noise distribution.

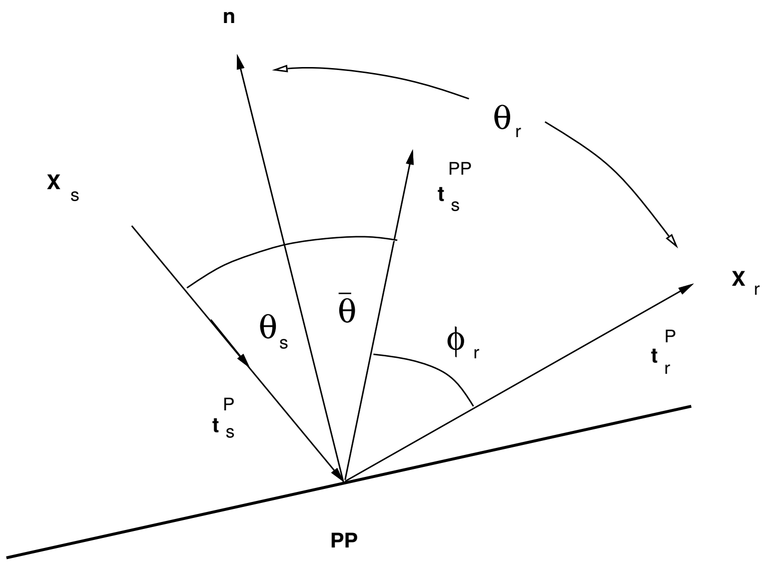

Figure 9: Generalized ray reflection and diffraction angle geometries. david2-anglegeom [NR]

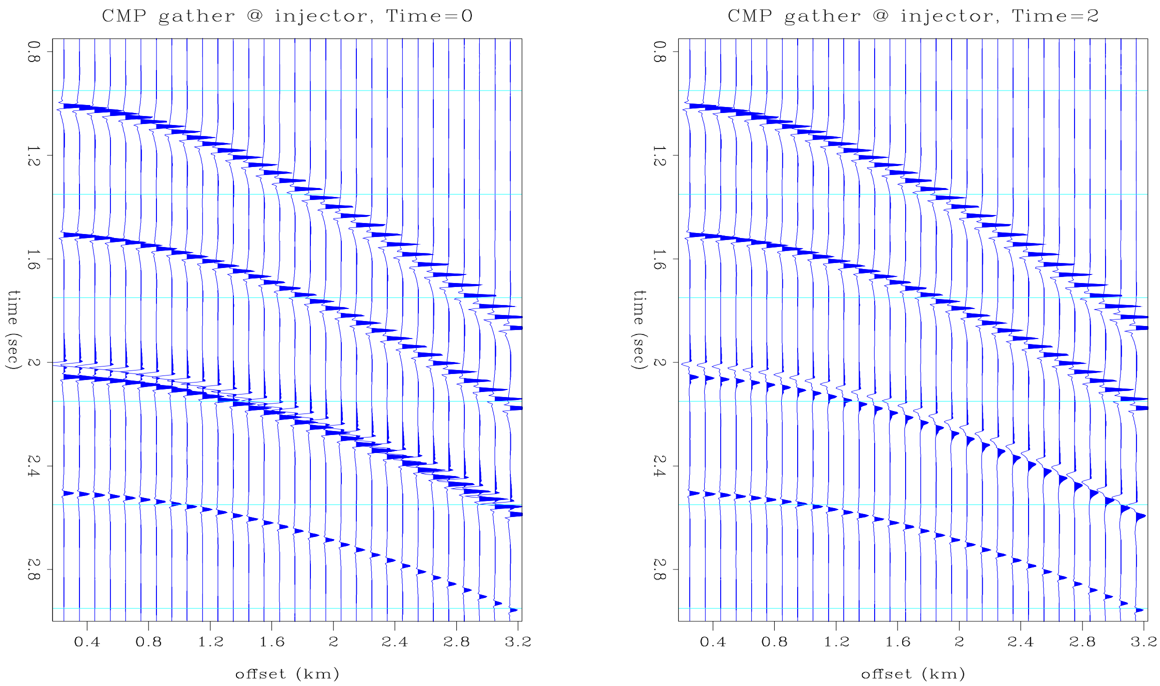

Figure 10: Noise-free CMP gathers co-located at a water injection well. The reservoir reflections are at 2 seconds traveltime. Pre-flood (left panel), the reflections and AVO response are strong. Post-flood, the reflections and AVO response are weak. david2-clean12 [CR]

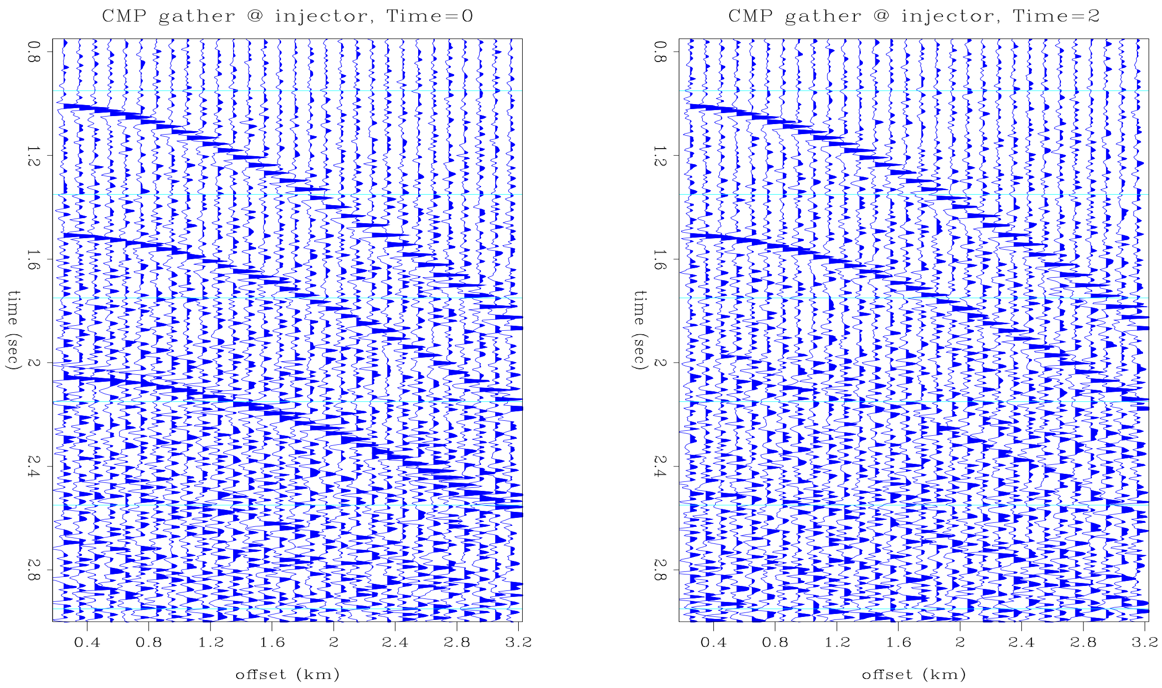

Figure 11: Same as previous figure but with added Gaussian noise, filtered to the signal bandwidth of 10–60 Hz. S/N is 2:1 at the reservoir reflection pre-flood, and 1:1 post-flood. david2-noise12 [CR]

SEISMIC DATA ANALYSIS

We generated 121 60-fold CMP gathers above the reservoir for each of the three waterflood phases. The shot spacing was 25 m and the offset spacing was 50 m. Pressure data were collected in marine streamer geometry with a near offset of 250 m and a maximum offset of 3.2 km. The traces were generated with a record length of 4 seconds at a 4 ms sample interval, with signal content in the 10–60 Hz frequency bandwidth. Random, Gaussian distributed noise was added to each trace independently for each of the three simulated surveys, with a 2:1 S/N ratio at the reservoir reflection pre-flood, and a 1:1 S/N ratio post-flood. This provided us with three synthetic prestack time-lapse seismic monitor surveys with which we analyzed for signs of waterflood activity.

Stacked sections

Figure **??** shows the stacked section from the base survey, before any water injection. The plot is enlarged to focus on the reservoir reflections at 2 km depth. Stacked reflection amplitudes are roughly proportional to the P impedance contrast at a reflector, as long as no anomalous AVO is present. Before waterflood, there are no lateral variations in stacked reflection character along the reservoir, except those due to the added noise. Figure **??** shows the stacked section from the survey after one time step of waterflood injection. There is some slight dimming in the stacked reflection amplitude centered about the well locations at 2 and 3 km distance along the line. Figure **??** shows the stacked section from the survey generated after two time steps of waterflood. The dimming in reflection character is more apparent than after the first waterflood, since the water invasion zone has expanded to a greater distance, thereby creating a larger zone of lowered P impedance contrast. Figure **??** shows a close-up of the stacked data at reservoir depth, showing more clearly the dimming and lateral spread of stacked reflection amplitudes due to the diffusive waterflood.

Figure **??** shows the stacked difference section, obtained by subtracting the stacked pre-flood base section from the stacked waterflood section after one time step. The zones of water invasion are clearly evident in that they give rise to differential reflections, including diffusive diffraction tails at the diffuse edge of the water slug front. Figure **??** shows the stacked difference section comparing the base pre-flood survey to the survey taken after two time steps of waterflood. The water invasion zone looks larger in spatial extent and therefore stronger in amplitude. Again, some diffuse diffractions are evident at the edge of the waterflood. We note that the stacked sections contain poor lateral resolution of the waterflood front because the stacked reflections are smeared laterally over a large Fresnel zone. Prestack wave-equation migration of the raw CMP data can collapse the Fresnel zone down to a spatial resolution on the order of a dominant seismic wavelength, i.e., from hundreds of meters unmigrated to tens of meters after migration.

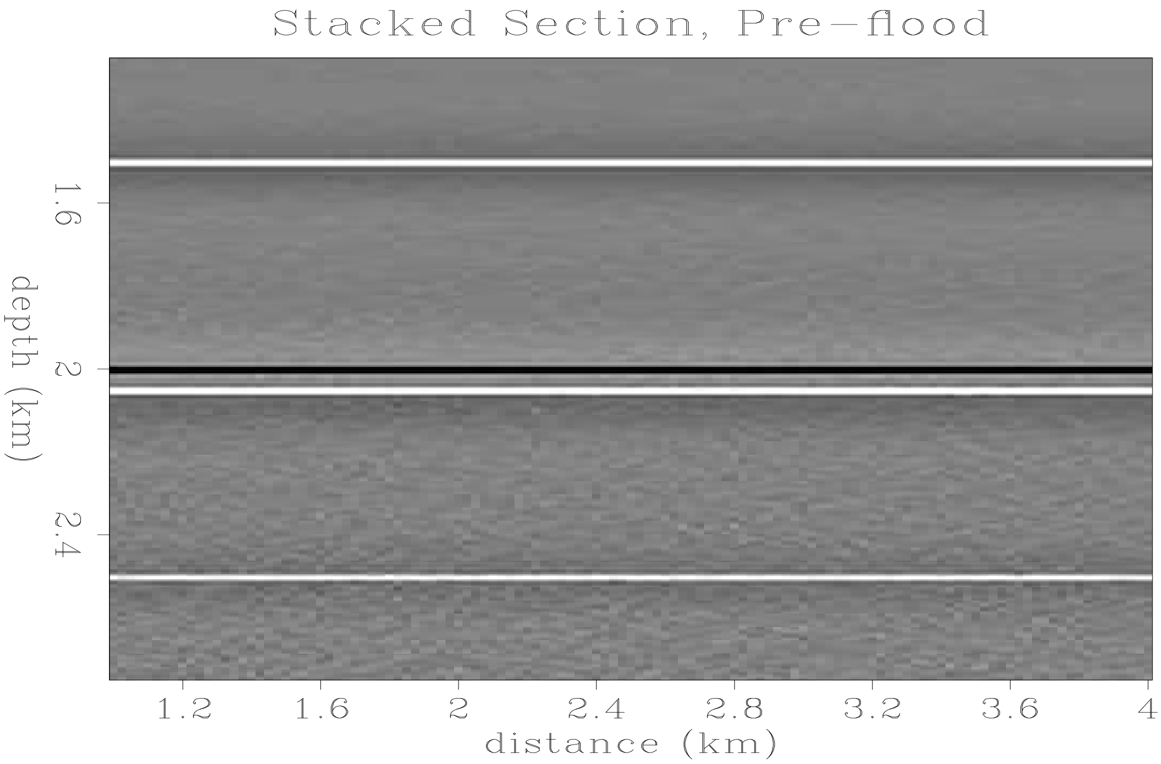

Figure 12: Pre-flood stacked section. david2-stack1 [CR]

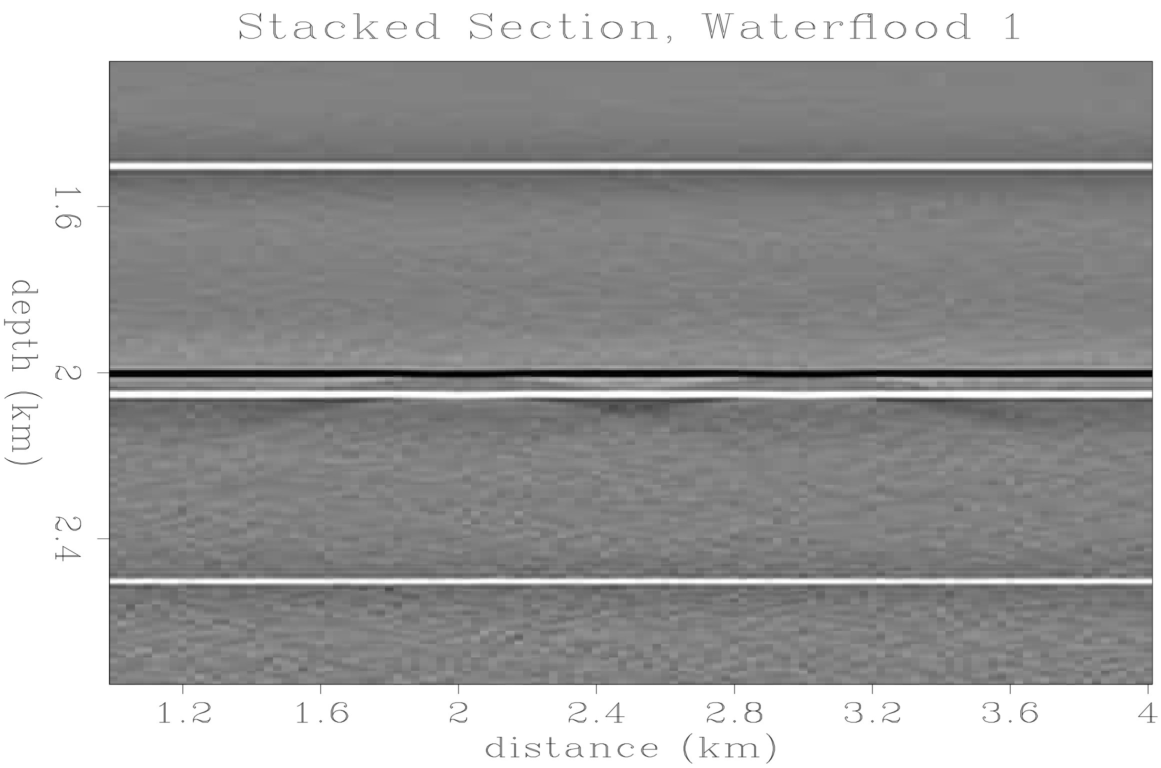

Figure 13: Waterflood 1: stacked section. david2-stack2 [CR]

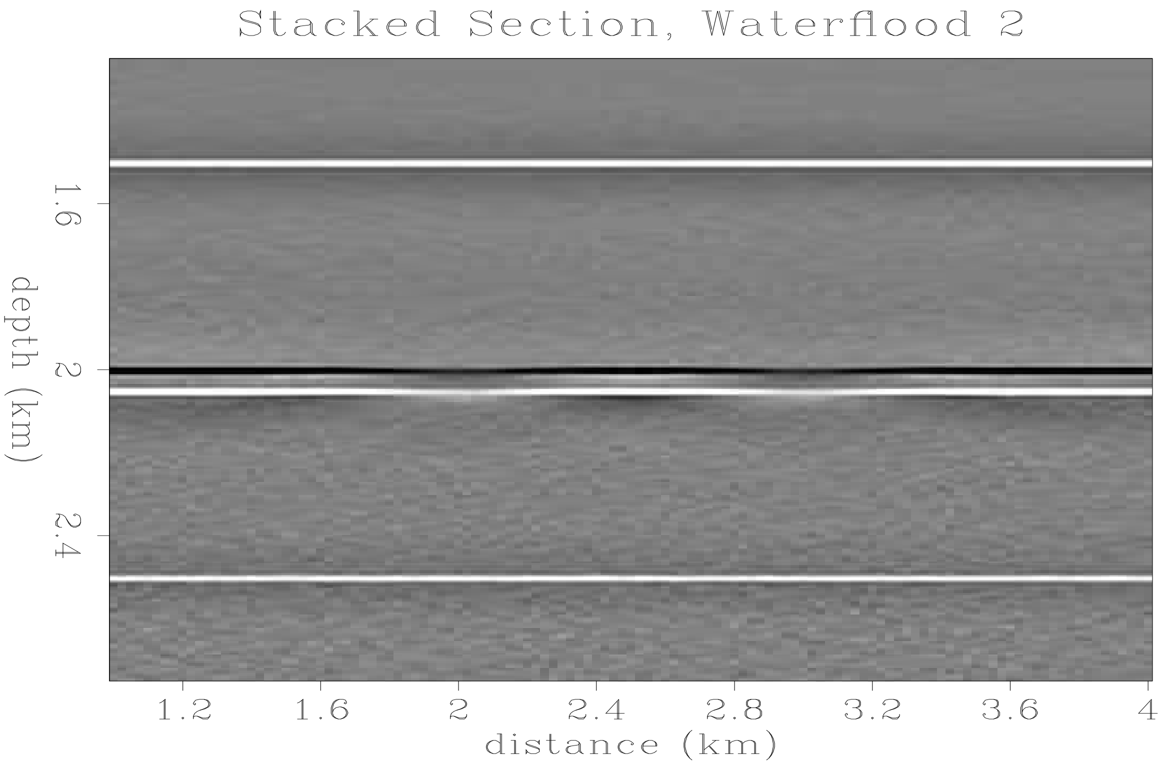

Figure 14: Waterflood 2: stacked section. david2-stack3 [CR]

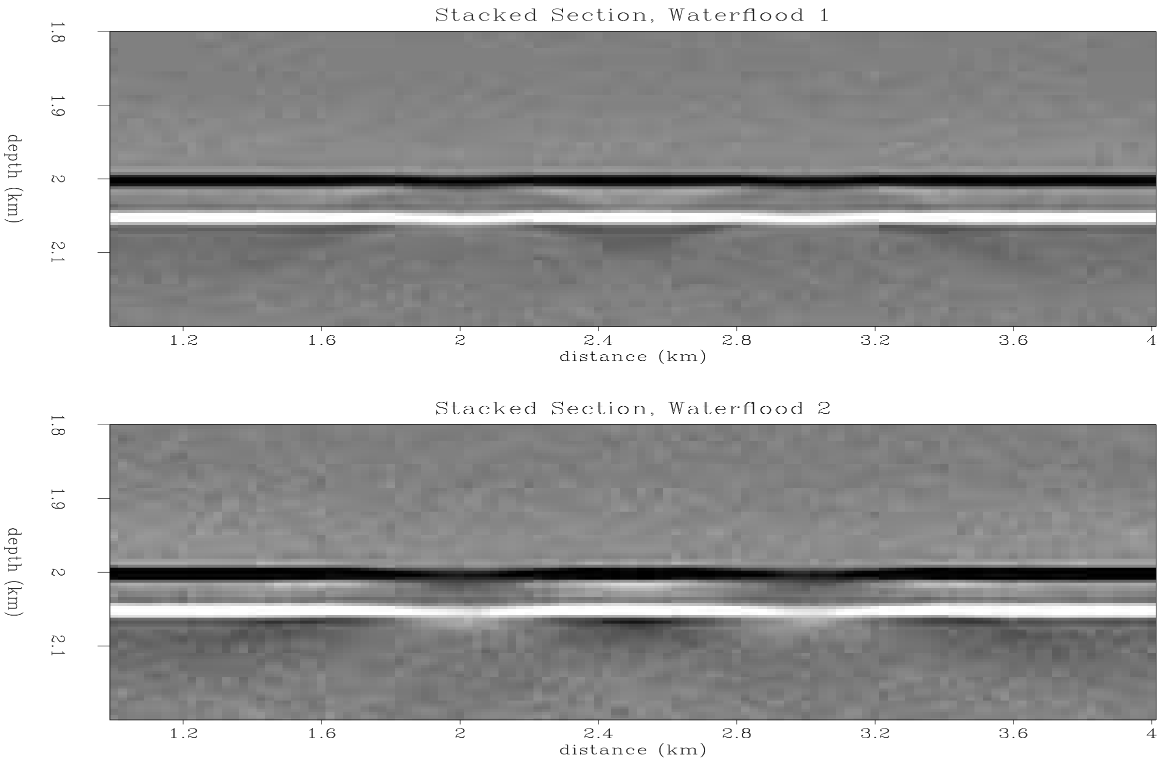

Figure 15: Waterflood 1 & 2 stacked sections. david2-stack23 [CR]

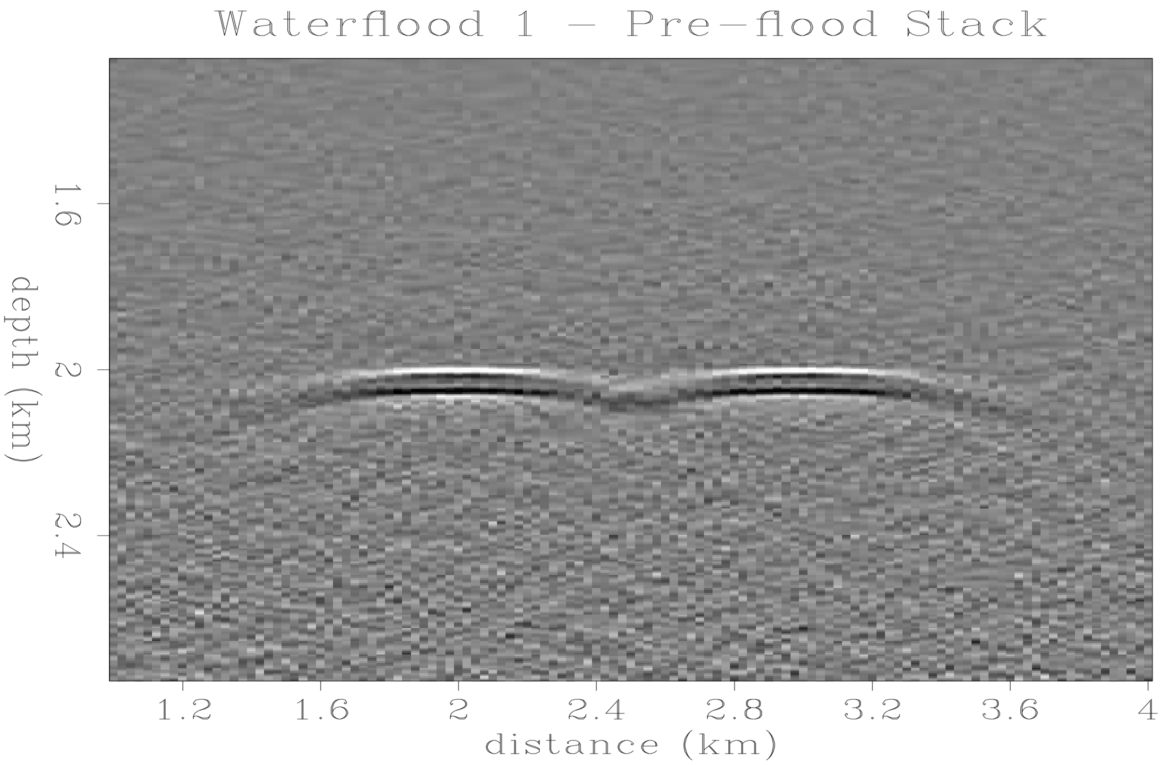

Figure 16: Waterflood 1 - Base stacked difference section. david2-stack12 [CR]

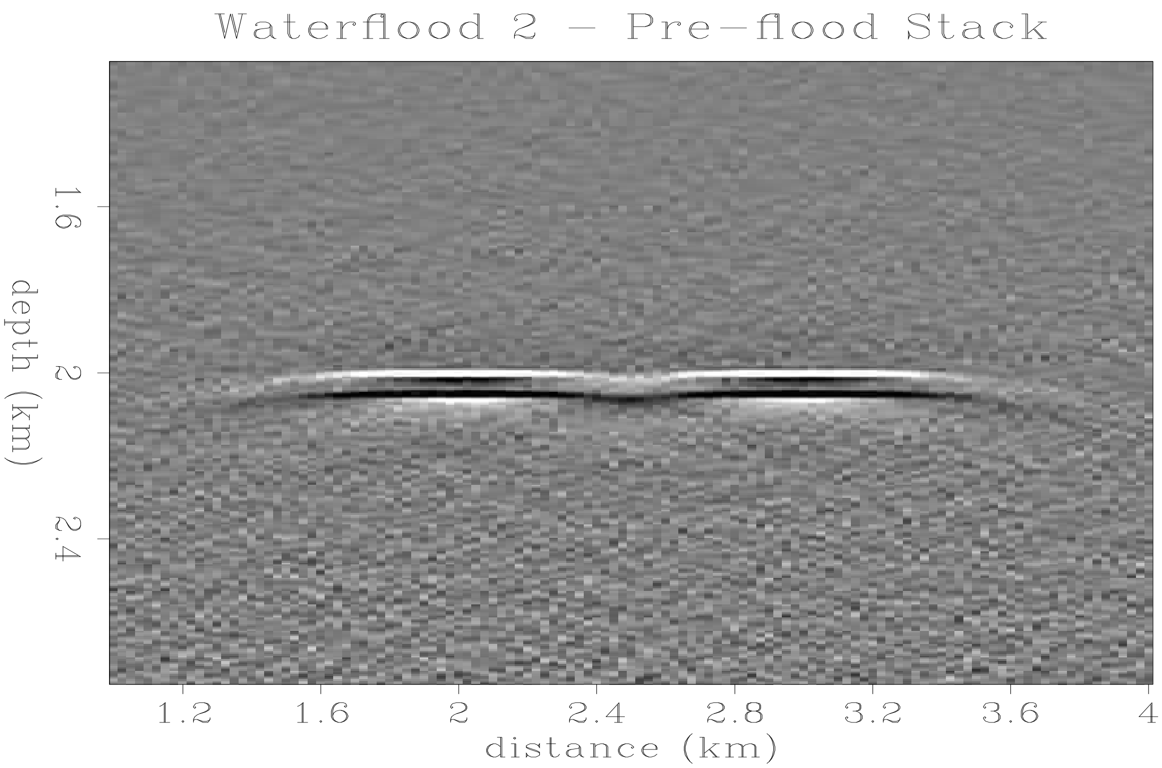

Figure 17: Waterflood 2 - Base stacked difference section. david2-stack13 [CR]

Prestack migrated sections

Figure **??** shows the prestack migrated section corresponding to the survey after the first time step of waterflood. Figure **??** shows the same for the survey after two time steps of waterflood. The dimming of the reflection events at the reservoir depths of 2 km is imaged more clearly than on the stacked sections, and the lateral and vertical resolution is better. This increase in apparent resolution results from the Fresnel zones having been collapsed to a spatial wavelength, and the diffraction tails having been correctly positioned at the diffuse edges of the water invaded zone.

Figure **??** shows a close up of the reservoir zone prestack migrations after one and two time steps of waterflood. This plot should be compared with the stacked section counterpart in Figure **??**. The prestack migrated images show more correct amplitude variation and lateral extent than the stacked images, as is physically intuitive.

Figure **??** shows the difference section of the prestack migrated sections before and after one time step of water injection. This figure can be compared directly to the stacked section counterpart of Figure **??**. Note that the diffraction tails have been collapsed, and the spatial resolution is good enough to closely match the true extent of the P impedance water invasion zone as depicted in the true model of Figures **??** and **??**. Figure **??** shows the difference section of the prestack migrated sections before and after two time steps of water injection. This figure can be compared directly to the stacked section counterpart of Figure **??**. Again, the diffractions have been correctly positioned to image the diffusive edge of the water slug, and the spatial resolution has increased from a Fresnel width down to a seismic wavelength. Note that the boundary of the migrated reflections match closely with the P and S impedance fronts in the true models of Figures **??** and **??**.

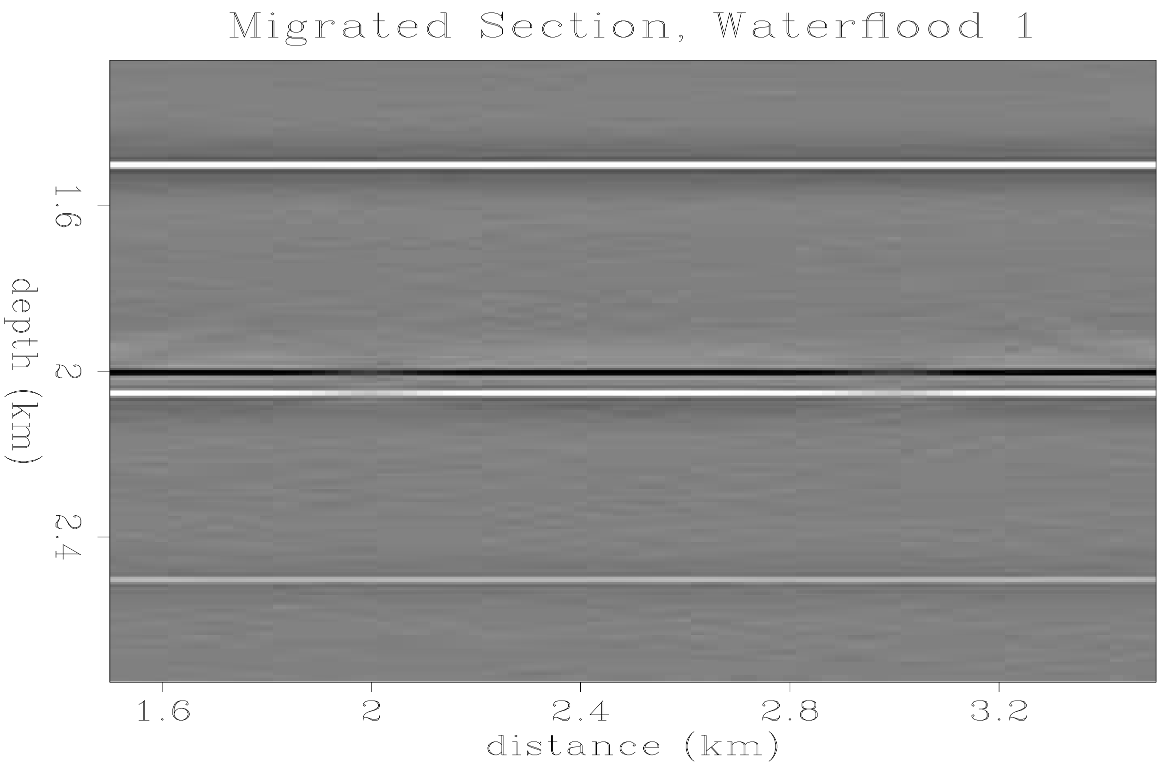

Figure 18: Waterflood 1: migrated section. david2-mig2 [CR]

Prestack impedance inversions

We perform a prestack seismic impedance inversion on each of the three synthetic surveys. The basis of the method is outlined here, and given in more detail in Lumley and Beydoun (1991), and Lumley (1993). The first step consists of estimating angle-dependent reflectivity via a true-amplitude least-squares Kirchhoff prestack migration. This is obtained by an l_2 estimate of the $\grave{P}\acute{P}$ coefficient in constant offset sections at each subsurface point:

$$\grave{P}\acute{P}(\mathbf{x};\mathbf{x}_h) \approx \frac{\int_\omega \int_{\mathbf{x}_m} ik\, A_s A_r D e^{-i\omega\tau_{sr}}\, d\mathbf{x}_m\, d\omega}{\int_\omega \int_{\mathbf{x}_m} k^2 A_s^2 A_r^2\, d\mathbf{x}_m\, d\omega + \epsilon^2(\mathbf{x};\mathbf{x}_h)}\ , \tag{14}$$

and a separate l_1 estimate of the reflection angles $\bar{\theta}$ directly from the data in constant offset sections at each subsurface point:

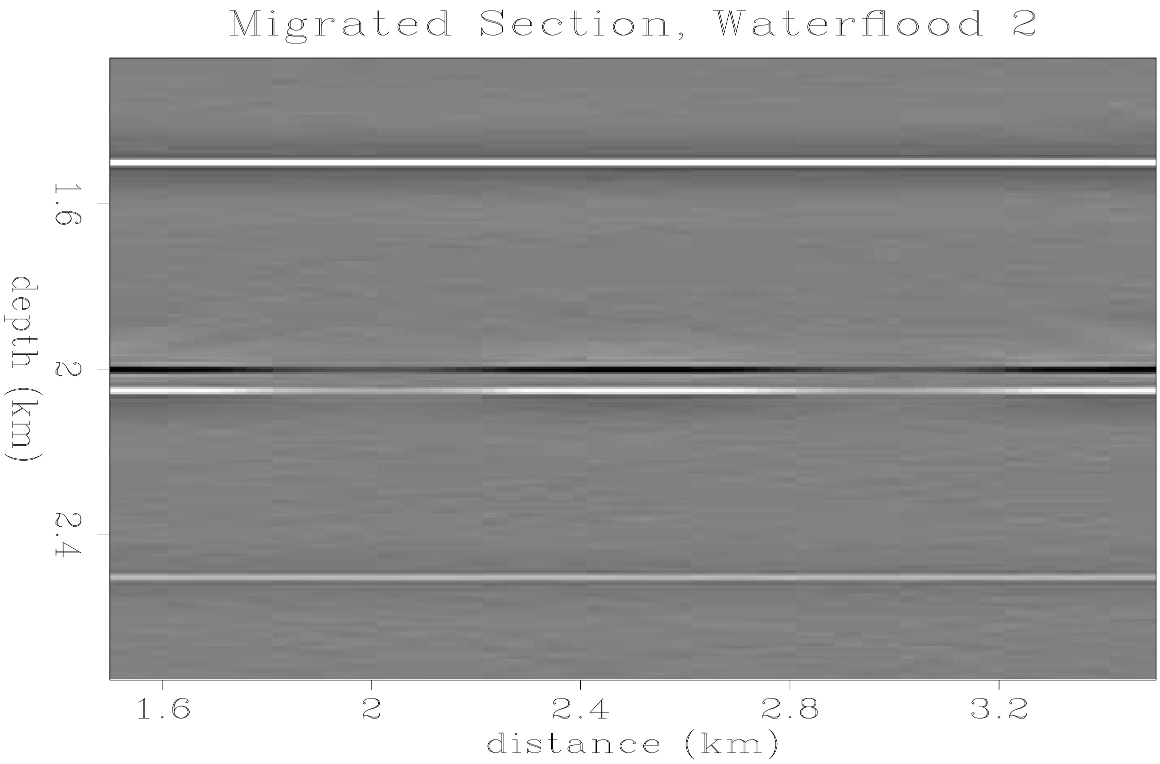

Figure 19: Waterflood 2: migrated section. david2-mig3 [CR]

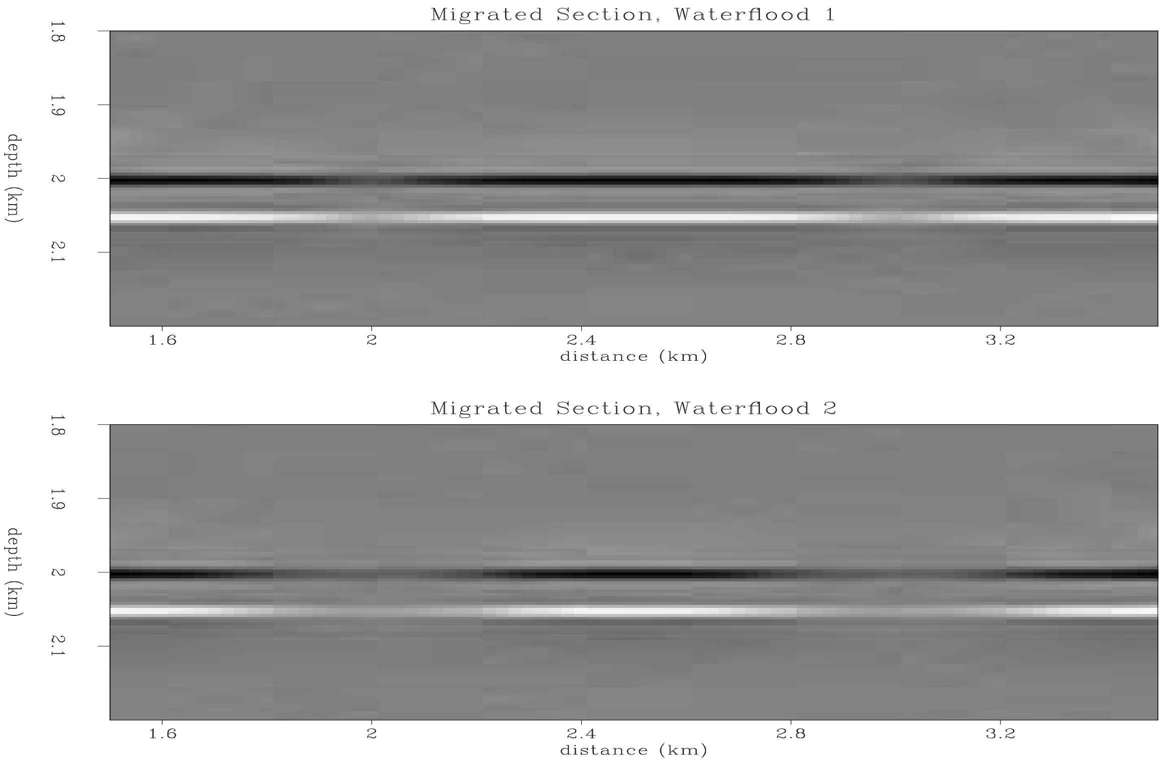

Figure 20: Waterflood 1 & 2: migrated sections. david2-mig23 [CR]

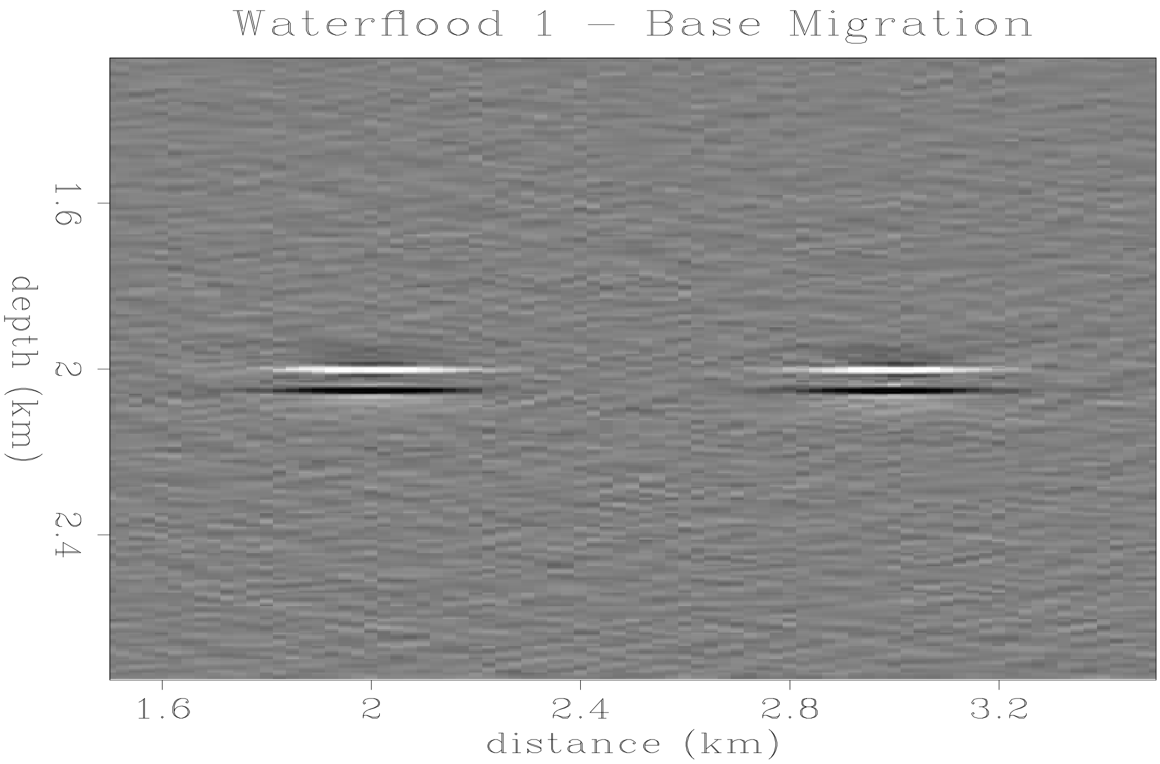

Figure 21: Waterflood 1 - Base migrated difference section. david2-mig12 [CR]

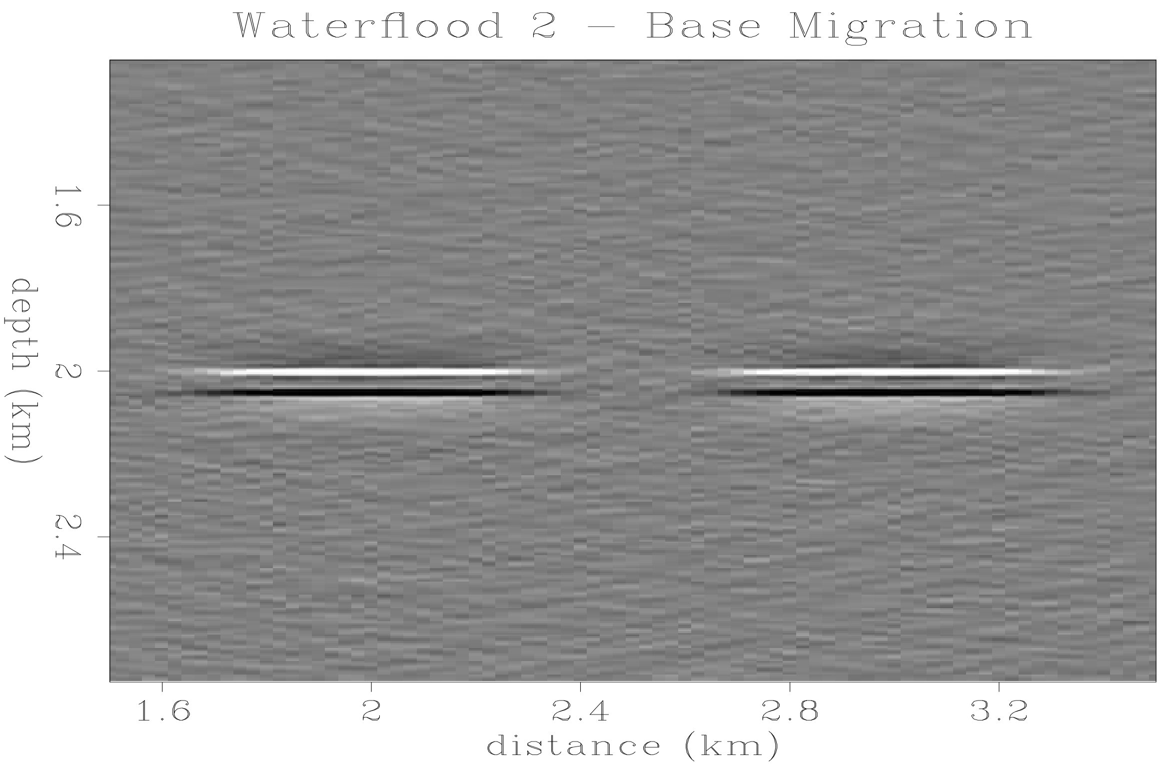

Figure 22: Waterflood 2 - Base migrated difference section. david2-mig13 [CR]

$$\cos 2\bar{\theta}(\mathbf{x};\mathbf{x}_h) \approx \frac{\int_\omega \int_{\mathbf{x}_m} |D| e^{-i\omega\tau_{sr}} \cos\theta_{sr}\, d\mathbf{x}_m\, d\omega}{\int_\omega \int_{\mathbf{x}_m} |D| e^{-i\omega\tau_{sr}}\, d\mathbf{x}_m\, d\omega + \epsilon^2(\mathbf{x};\mathbf{x}_h)} , \tag{15}$$

where D are the recorded seismic data. To complete the final estimation of $\grave{P}\acute{P}(\bar{\theta})$, we make a simple set of mappings from the separate estimates of $\grave{P}\acute{P}$ and $\bar{\theta}$. A map of $\bar{\theta}(\mathbf{x};\mathbf{x}_h)$ can be obtained directly as:

$$\mathcal{M}_1 \quad : \quad \cos\ 2\bar{\theta}(\mathbf{x};\mathbf{x}_h) \rightarrow \bar{\theta}(\mathbf{x};\mathbf{x}_h) . \tag{16}$$

Then, since there is a one-to-one mapping of $\bar{\theta}$ to any point $(\mathbf{x};\mathbf{x}_h)$, and $\grave{P}\acute{P}$ to the same point $(\mathbf{x};\mathbf{x}_h)$, there is a unique map of $\grave{P}\acute{P}(\mathbf{x};\mathbf{x}_h)$ and $\bar{\theta}(\mathbf{x};\mathbf{x}_h)$ to $\grave{P}\acute{P}(\bar{\theta}(\mathbf{x}))$ such that:

$$\mathcal{M}_2 \quad : \quad \{\grave{P}\acute{P}(\mathbf{x};\mathbf{x}_h), \bar{\theta}(\mathbf{x};\mathbf{x}_h)\} \rightarrow \grave{P}\acute{P}(\bar{\theta}(\mathbf{x})) , \tag{17}$$

which is the desired result. This completes the angle-dependent reflectivity estimation process.

Once we have estimated $\grave{P}\acute{P}(\bar{\theta}(\mathbf{x}))$, an inverse problem for three isotropic elastic parameters can be posed. Under the assumption that *relative contrasts* in material properties are small at reflecting boundaries, and the reflection angles are well within the pre-critical region (Aki and Richards, 1980), a linearization of the Zoeppritz plane wave reflection coefficients can be made at every subsurface point $\mathbf{x}$:

$$\grave{P}\acute{P}(\bar{\theta}) \approx I_p c_1(\bar{\theta}) + I_s c_2(\bar{\theta}) + D c_3(\bar{\theta}) , \tag{18}$$

where $\{I_p, I_s, D\}$ are the relative contrasts in P impedance, S impedance and density at the reflecting boundary, and $\{c_1, c_2, c_3\}$ are known basis functions which are analytical in $\bar{\theta}$. The three basis functions are plotted in Figure **??**, with c_1 at the top, c_2 at the bottom, and c_3 near the zero axis in the middle, and are given here analytically as:

$$\begin{aligned} c_1 &= 0.5 \sec^2 \bar{\theta} \\ c_2 &= -4\gamma^2 \sin^2 \bar{\theta} \\ c_3 &= 2\gamma^2 \sin^2 \bar{\theta} - 0.5 \tan^2 \bar{\theta} \end{aligned} \tag{19}$$

where γ is the shear to compressional velocity ratio V_s/V_p. We invert (18) at every subsurface location $\mathbf{x}$ by a least-squares method which bootstraps with offset and angle. This yields an output section each of relative P and S impedance contrasts.

Figure **??** shows the P impedance inversion difference section for the two surveys before and after one time step of waterflood. The waterflood zone at the top of

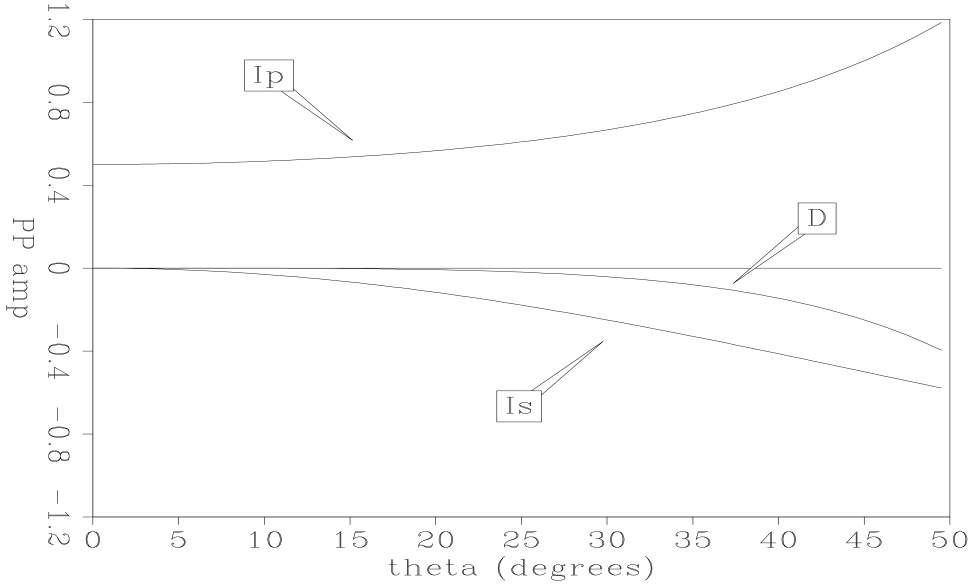

Figure 23: Elastic impedance parameterization. Reflectivity unit impulse radiation curves (basis functions) $\{c_1, c_2, c_3\}$ for the impedance parameter set $\{I_p, I_s, D\}$. The uppermost curve is due to a unit perturbation in relative P impedance contrast alone, the lower curve is due to a unit perturbation in relative S impedance contrast alone, and the middle curve is due to a unit perturbation in relative density contrast alone. david2-imprad-ann [NR]

the reservoir shows the correct increase in P impedance at the well location due to injection of water which is of higher P impedance than the initial light oil in place at lower pore pressure. Figure **??** shows the impedance inversion difference section for the two surveys before and after two time steps of waterflood production. Again, the waterflood zone at the top of the reservoir shows the correct increase in P impedance at the well, and the correct lateral spatial extent. We note that these P impedance sections resemble the migrated sections because, to first order, a (migrated) stack approximates the normal incidence P-P reflection coefficient in the absence of anomalous AVO. However, the impedance inversion results are more accurate in terms of relative impedance contrast estimates than a simple prestack imaging algorithm in general.

Figure **??** shows the S impedance inversion difference section for the two surveys before and after one time step of waterflood. The waterflood zone at the top of the reservoir shows the correct decrease in S impedance at the well location due to injection of water which is of lower S impedance than the initial light oil in place at lower pore pressure. However, the S impedance results are much noisier than the P impedance results, which is expected since they are most sensitive to the relatively fewer far offset trace data. Figure **??** shows the S impedance inversion difference section for the two surveys before and after two time steps of waterflood production. Again, the waterflood zone at the top of the reservoir shows the correct decrease in S impedance at the well, and the correct lateral spatial extent, although in a somewhat more noisy manner.

Finally, the impedance inversions detected the correct opposite polarity changes in P and S impedance between the pre-waterflood survey and the post-waterflood surveys. These two parameters, instead of one single (potentially ambiguous) migrated or stacked reflection amplitude parameter, may be more diagnostic of changes in reservoir petrophysical properties over time-lapse monitor surveys. Furthermore, the magnitude of the impedance changes was recovered reasonably well in data having a significant noise level, since the change in S impedance between surveys is estimated from the data to be on the order of 1.5 times the magnitude of the change in the P impedance after waterflood production. Estimates of absolute or relative changes in the petrophysical properties themselves could be a very valuable tool in monitoring reservoir production processes.

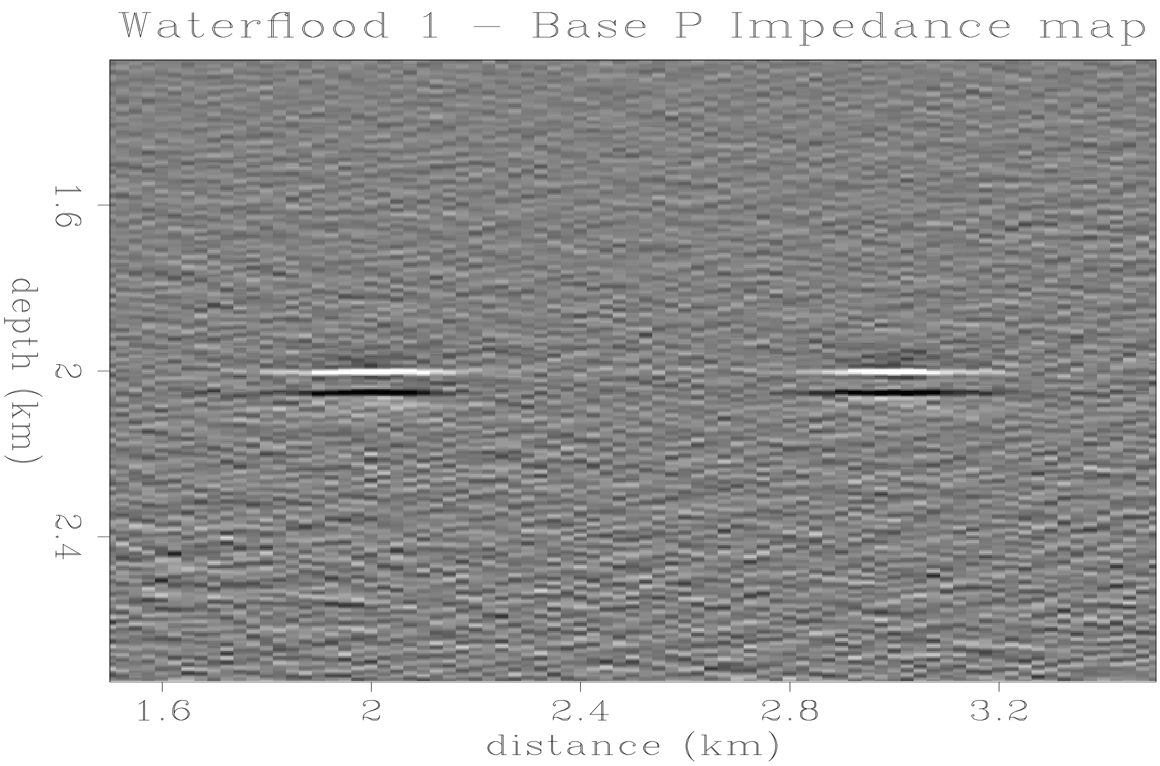

Figure 24: Waterflood 1 - Base P-impedance difference section. $\boxed{\text{david2-Pimp12}}$ [CR]

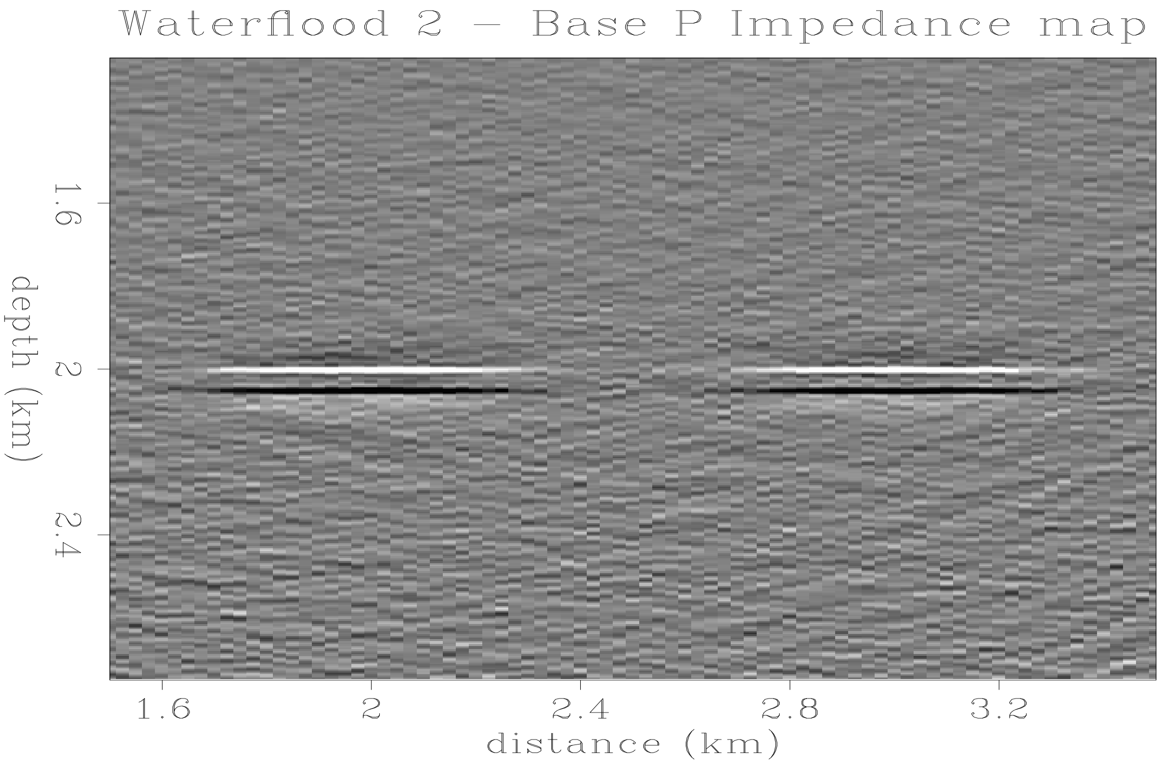

Figure 25: Waterflood 2 - Base P-impedance difference section. david2-Pimp13 [CR]

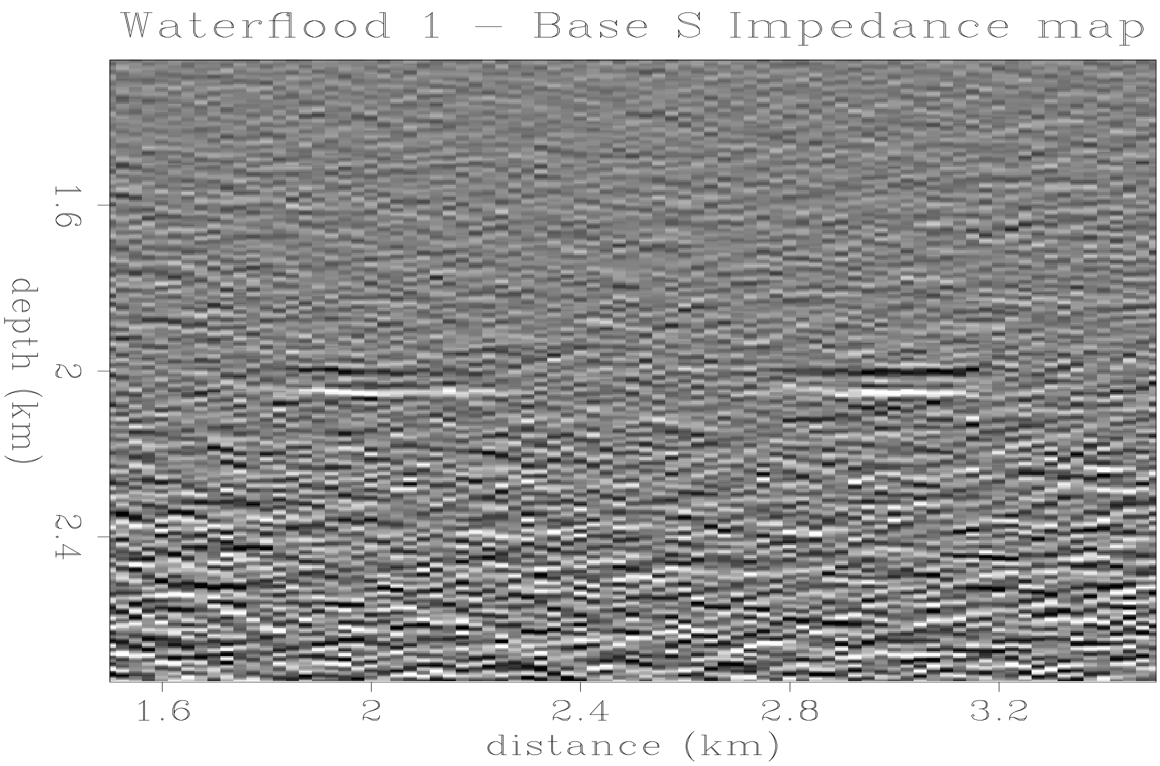

Figure 26: Waterflood 1 - Base S-impedance difference section. david2-Simp12 [CR]

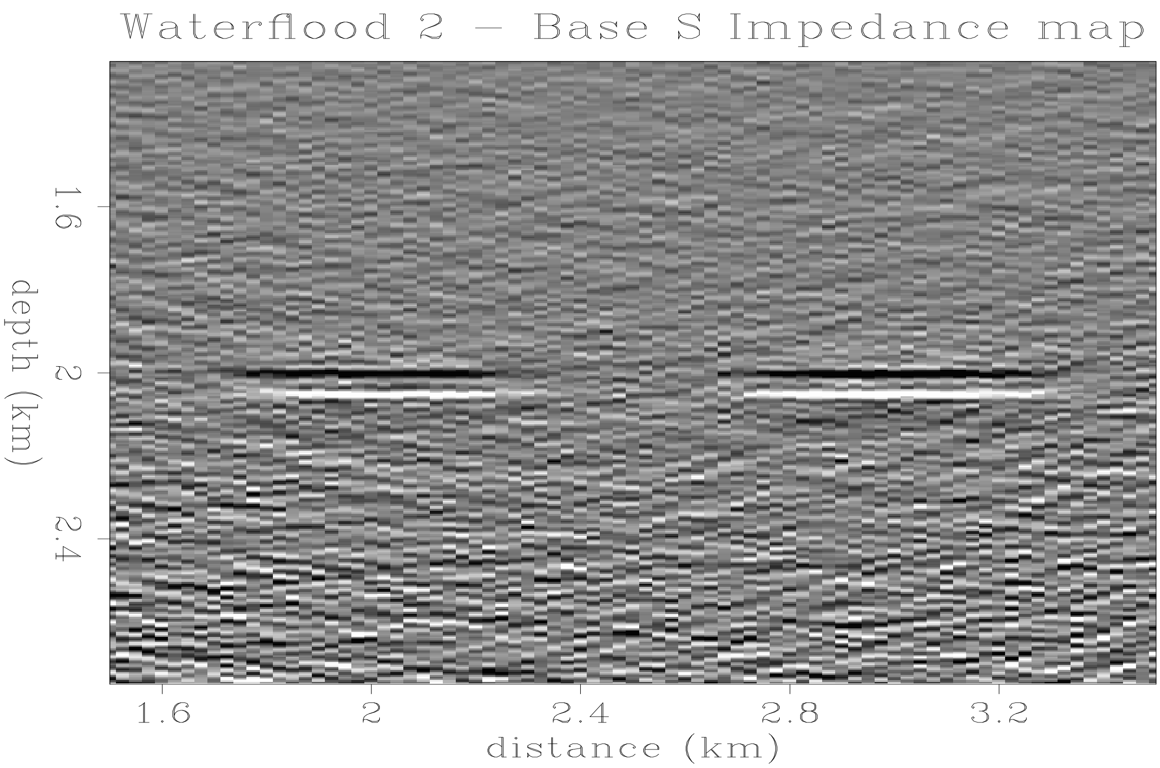

Figure 27: Waterflood 2 - Base S-impedance difference section. david2-Simp13 [CR]

CONCLUSIONS

We performed a model study to simulate waterflood production in a light oil reservoir of Ottawa sand, and generate synthetic time-lapse monitor seismic data both pre-flood, and at two subsequent waterflood phases. Pore pressure and oil/water pore saturation levels are simulated in the reservoir due to two water injection well galleries by diffusive fluid flow modeling. The pressure and saturation data are converted to rock density and both bulk and shear moduli, using rock physics calibration curves derived from laboratory data. Synthetic seismic reflection data are generated from the resulting spatially variable rock physics properties at three separate waterflood stages. In the presence of realistic noise levels, stacked and prestack migrated reflection images clearly show the extent of the water-invaded zone after production. Furthermore, we apply a prestack seismic impedance inversion method and accurately track the relative P and S impedance changes in the reservoir rock caused by the varying petrophysical conditions associated with the waterflood production process.

REFERENCES

Aki, K., and Richards, P. G., 1980, Quantitative seismology: W. H. Freeman and Company.

Bourbié, T., Coussy, O., and Zinszner, B., 1987, Acoustics of porous media: Gulf Publishing Company, Houston.

Dake, L. P., 1978, Fundamentals of reservoir engineering: Elsevier.

Gassmann, F., 1951, Über die elastizität poröser medien: Veirteljahrsschrift der Naturforschenden Gesellschaft in Zürich, **96**, 1–23.

Graebner, R., 1993, Geophysics: The potential and limits for reservoir description and monitoring: presented at the 1993 Annual Summer Research Workshop, Soc. Expl. Geophys..

Greaves, R. J., and Fulp, T. J., 1987, Three-dimensional seismic monitoring of an enhanced oil recovery process: Geophysics, **52**, 1175–1187.

Han, D., 1986, Effects of porosity and clay content on acoustic properties of sandstones and unconsolidated sediments: Ph.D. Thesis, Stanford University.

Lumley, D. E., 1993, Kirchhoff prestack impedance inversion: a gas reservoir pilot study: Stanford Expl. Proj. Report, **77**, Stanford University, 211–230.

Lumley, D. E., and Beydoun, W. B., 1991, Elastic parameter estimation by Kirchhoff prestack depth migration/inversion: Stanford Expl. Proj. Report, **70**, Stanford University, 165–192.

Lumley, D. E., and Beydoun, W. B., 1993, Angle-dependent reflectivity estimation by Kirchhoff migration/inversion: Stanford Expl. Proj. Report, **79**, Stanford University.

Nur, A., 1989, Four dimensional seismology and (true) direct detection of hydrocarbons: The petrophysical basis: The Leading Edge, **9**, 30–36.

Pullin, N. E., Jackson, R. K., Matthews, L. W., Thorburn, R. F., Hirsche, W. K., and den Boer, L. D., 1987, 3-D Seismic Imaging of Heat Zones at an Athabasca Tar Sands Thermal Pilot: 57th Annual Internat. Mtg., Soc. Expl. Geophys., Expanded Abstracts, 391–394.